Numerical modelling of structural vibration with piece-wise constant material properties using the nodal discontinuous Galerkin method

Indra Sihar[1,2*]**, Jieun Yang**[2]**, Maarten Hornikx**[2]

[1]Department of the Built Environment, Eindhoven University of Technology, Eindhoven, The Netherlands.
[2]Engineering Physics, Institut Teknologi Bandung, Bandung, Indonesia.

*{i.sihar@tue.nl}

Abstract

In this work, vibrations of complex structures excited by an impact source are modelled using the time domain nodal discontinuous Galerkin (DG) method, which solves linear elasticity equations. Two structures of interest, a T-shaped structure and a scaled lightweight wooden floor (LWF), are taken as example cases. Both structures consist of components that differ in their mechanical properties. Rankine-Hugoniot jump conditions for piece-wise constant material properties are used to obtain accurate numerical fluxes in the DG method. Free or fixed boundary conditions are imposed on the surfaces of the structures. Furthermore, constant viscous damping forces are added to the model to create vibrational energy losses of the structure. To validate the numerical results, the mobility of the structures is calculated and compared with experimental data. The agreement is good regarding the natural frequencies, with a maximum difference of less than 4 % for the T-shaped structure in the range below 500 Hz, and 6.4 % for the scaled LWF in the range below 300 Hz. The adopted damping approach is shown to be insufficient to represent a broad frequency range.

Keywords: discontinuous Galerkin, vibration, linear elasticity, wooden structures.

1 Introduction

Due to the increasing focus on sustainability issues with conventional concrete-based construction methods, wood-based building methods have steadily gained more ground. However, these wooden building methods suffer from poor sound insulation in the low-frequency range due to the low weight of building components. Structural motions induced by human activity or mechanical systems can excite vibrations in structures. These vibrations transmit through the building elements and subsequently radiate low-frequency noise that causes disturbance to the occupants of the building.

Two common structures found in wooden-based buildings are T-shaped structures or lightweight wooden floors (LWF). To limit the noise and vibration levels transmitted through such structures, it is important to accurately predict the level of vibration in the structures. One of the vibration models of the T-shaped structure was developed in Ref. [14] using the plate theory, considering both out-of-plane and in-plane vibrations. Some models have been developed to predict the LWF vibration field utilising Kirchhoff plate and Euler beam vibration theories. These models were solved using the modal expansion method, as shown in Ref. [2]. A recent review [5] showed that the LWF vibration model can be refined using the more general plate and beam vibration models, such as Mindlin plate and Timoshenko beam theories. The analytical solutions of these methods, however, are only possible for specific geometries, boundary conditions, and homogeneity of material properties. To determine the transmission of vibration through complex systems, energy-based methods or wave-based methods are commonly used. [3, 4].

The energy-based methods include statistical energy analysis (SEA), which is mainly used at high frequencies where the vibration modal density is high. This method has been applied successfully to analyse vibration transmission of coupled masonry and concrete walls [7]. These approaches are often preferable

since they provide a quick solution or when the detailed information on the structure is not demanded, e.g., octave band analysis. However, energy-based methods fail in the low-frequency region, which is important for vibration problems in building acoustics applications. Measurement results have shown that the impact sound levels of an LWF structure are dominant below 100 Hz [9].

Wave-based methods are numerical methods that solve the governing equations that describe structural vibration, and this category is usually used for the low-frequency range. There are several wave-based numerical methods used to predict the vibration field of building elements, such as the finite element method (FEM) [8], the finite difference time domain (FDTD) method [13], the spectral finite element method (SFEM) [12], and the discontinuous Galerkin (DG) method [16]. Among these methods, the DG method is a relatively new method adapted to the vibration problem. This method has certain advantages compared to the other wave-based methods. For example, it can represent the problem domain using unstructured mesh elements to easily deal with a complex domain, and it allows refinement of the solution by increasing the polynomial order or element number. Another advantage is that the DG method solves the governing equations using an element-wise formulation. Therefore, it provides a framework well suited for parallel computation. This allows for significantly accelerated calculations [11]. This method has been extensively studied for application in another area of applied physics as seismology [19]. However, its application to structural vibration is still in its infancy. So far, the DG method has been applied to a forced vibration problem of a concrete slab and an L-shaped structure [16]. However, this application was limited to homogeneous material properties.

In this work, the time domain nodal DG method is applied to the vibration of the T-shaped and LWF structures that have components with different material properties. This study aims to apply the nodal DG method to the vibration problem of solid structures with piece-wise constant material properties. The proposed model is based on a 3-D solid domain, while other methods usually propose vibration models in reduced dimensions such as beams and plates [5]. Mobilities of the structures are determined using DG and compared with experimental results. The paper is organised as follows. Section 2 describes the computation methodology of the nodal DG method. Section 3 shows the details of the case studies along with their excitation and receivers locations. The measurement set-up for validating the result is shown in section 4. Section 5 shows and discusses the numerical simulation and measurement results, and section 6 concludes the paper.

2 Computational Methodology

2.1. Linear elasticity equations

The linear vibration of a structure can be modelled using the linear elasticity equations, which governs the propagation of elastic waves in a solid medium. This set of equations consists of the mass conservation, the momentum conservation, and Hooke's constitutive equations [10]. For a Cartesian 3-D coordinate system, the equations for an isotropic medium can be written as a set of linear first-order hyperbolic equations in a velocity-stress form as:

$$\frac{\partial \mathbf{q}}{\partial t} + \nabla \cdot \mathbf{F}(\mathbf{q}) = \frac{\partial \mathbf{q}}{\partial t} + \mathbf{A}_j \frac{\partial \mathbf{q}}{\partial x_j} = \mathbf{g} - \zeta \mathbf{q}, \tag{1}$$

$$\mathbf{q}(\boldsymbol{x}, t) = \begin{bmatrix} u & v & w & \sigma_{xx} & \sigma_{yy} & \sigma_{zz} & \sigma_{xz} & \sigma_{yz} & \sigma_{xy} \end{bmatrix}^T,$$

$$\mathbf{g}(\boldsymbol{x}, t) = \begin{bmatrix} g_x & g_y & g_z & 0 & 0 & 0 & 0 & 0 & 0 \end{bmatrix}^T,$$

$$\zeta = \mathrm{diag}\begin{pmatrix} \zeta_x & \zeta_y & \zeta_z & 0 & 0 & 0 & 0 & 0 & 0 \end{pmatrix},$$

where u, v, w are the velocities in the x-, y-, and z- directions, respectively. $\sigma_{xx}, \sigma_{yy}, \sigma_{zz}, \sigma_{xz}, \sigma_{yz}, \sigma_{xy}$ are the normal and shear stress components, g_x, g_y, g_z are the body forces, and $\zeta_x, \zeta_y, \zeta_z$ are the viscous damping forces. The flux matrix reads $\mathbf{F}(\mathbf{q}) = [\boldsymbol{f}_x, \boldsymbol{f}_y, \boldsymbol{f}_z] = [\mathbf{A}_x \mathbf{q}, \mathbf{A}_y \mathbf{q}, \mathbf{A}_z \mathbf{q}]$. The constant flux Jacobian matrix $\mathbf{A}_j$ is

given as:

$$\mathbf{A}_j = \left[\begin{array}{c|c} \mathbf{0}_{3\times3} & \mathbf{A}_{1,j} \\ \hline \mathbf{A}_{2,j} & \mathbf{0}_{6\times6} \end{array} \right], \mathbf{A}_{1,j} = -\frac{1}{\rho} \left[\begin{array}{cccccc} \delta_{xj} & 0 & 0 & \delta_{zj} & 0 & \delta_{yj} \\ 0 & \delta_{yj} & 0 & 0 & \delta_{zj} & \delta_{xj} \\ 0 & 0 & \delta_{zj} & \delta_{xj} & \delta_{yj} & 0 \end{array} \right], \tag{2}$$

$$\mathbf{A}_{2,j} = - \left[\begin{array}{ccc} (\lambda + 2\mu)\delta_{xj} & \lambda\delta_{yj} & \lambda\delta_{zj} \\ \lambda\delta_{xj} & (\lambda + 2\mu)\delta_{yj} & \lambda\delta_{zj} \\ \lambda\delta_{xj} & \lambda\delta_{yj} & (\lambda + 2\mu)\delta_{zj} \\ \mu\delta_{zj} & 0 & \mu\delta_{xj} \\ 0 & \mu\delta_{zj} & \mu\delta_{yj} \\ \mu\delta_{yj} & \mu\delta_{xj} & 0 \end{array} \right], \tag{3}$$

where λ and μ are the Lamé parameters, ρ is the mass density and index j has components $[x, y, z]$. The δ_{ij} denotes the Kronecker delta function. The solution of Equation 1 consists of a linear combination of elastic waves propagating with longitudinal wave speed ($c_p = \sqrt{(\lambda + 2\mu)/\rho}$) and transverse wave speed ($c_s = \sqrt{\mu/\rho}$). The Lame parameters are represented by using Young's modulus (E) and Poisson's ratio (v) as $\lambda = Ev/(1 + v)(1 - 2v)$ and $\mu = E/2(1 + v)$.

2.2. Nodal discontinuous Galerkin method

The nodal discontinuous Galerkin (DG) method is used to solve Equation 1, and the algorithm of the nodal DG method developed by Hesthaven and Warburton [6] is adopted. The problem domain is approximated by the computational domain Ω_h with K number of non-overlapping rectilinear tetrahedral elements D^k as $\Omega_h = \cup_{k=1}^{K} D^k$. On each D^k, the local solution is expanded by a combination of nodal basis functions as:

$$\mathbf{q}_h^k(\mathbf{x}, t) = \sum_{i=1}^{N_p} \mathbf{q}_h^k(\mathbf{x}_i^k, t) l_i^k(\mathbf{x}), \tag{4}$$

where $\mathbf{q}_h^k(\mathbf{x}_i^k, t)$ are the unknown nodal values, $l_i^k(\mathbf{x})$ are the 3-D Lagrange interpolation polynomials based on the nodal points $\mathbf{x}_i$, and N_p is the number of nodal points. The global solution is approximated as the direct sum of the local solutions as $\mathbf{q}(\mathbf{x}, t) \approx \mathbf{q}_h(\mathbf{x}, t) = \oplus_{k=1}^{K} \mathbf{q}_h^k(\mathbf{x}, t)$. The closed expression of the Lagrange interpolation polynomials in tetrahedral elements is constructed by the products of the Jacobi polynomials of order N, and the distribution of nodal points follows the optimised Legendre-Gauss-Lobato (LGL) points over a tetrahedral element as presented in Ref.[6]. The number of nodal points per element is $N_p = (N + 1)(N + 2)(N + 3)/6$. In each element, the nodal basis functions are used to approximate the unknown variables and the body forces in Equation 1. Then the residuals of the approximations are multiplied by the test functions following the Galerkin method. By performing spatial integration by parts twice, the strong formulation of Equation 1 becomes the following form:

$$\int_{D^k} \left[\frac{\partial \mathbf{q}_h^k}{\partial t} + \nabla \cdot \mathbf{F}(\mathbf{q}_h^k) \right] l_i^k \mathrm{d}\mathbf{x} = \int_{D^k} (\mathbf{g}_h^k - \zeta \mathbf{q}_h^k) l_i^k \mathrm{d}\mathbf{x} - \int_{\partial D^k} \mathbf{n} \cdot \left[\mathbf{F}^* - \mathbf{F}(\mathbf{q}_h^k) \right] l_i \mathrm{d}\mathbf{x}, \tag{5}$$

where ∂D^k is the element surface, $\mathbf{g}_h^k$ is the approximated body force vector, and $\mathbf{n} = [n_x, n_y, n_z]$ is the outward normal vector of the element surface ∂D^k. The flux along the normal direction of the element surface is defined as $\mathbf{n} \cdot \mathbf{F} = (n_x \mathbf{f}_x + n_y \mathbf{f}_y + n_z \mathbf{f}_z)$, and the $\mathbf{F}^*$ is the numerical flux.

In the DG method, the numerical flux ensures continuity of the global solution. It is a function of the interior solution ($\mathbf{q}_h^-$), which is the solution within the element D^k, and the exterior solution ($\mathbf{q}_h^+$), which is the solution of the neighbouring elements around D^k. In this work, the upwind numerical flux is chosen as the numerical flux. The upwind numerical flux can be derived by solving the Riemann problem at the interface between two homogeneous media. This interface represents the faces of two neighbouring elements located at the same position. Consider that the interface is located at $\mathbf{x} = 0$. The properties of the medium (λ^-, μ^-, ρ^-) are those of the internal medium at $\mathbf{x} < 0$, and (λ^+, μ^+, ρ^+) are those of the adjacent one at $\mathbf{x} > 0$. The Riemann problem is a discontinuous initial value problem that happens at this interface as:

$$\mathbf{q}_h(\mathbf{x}, 0) = \begin{cases} \mathbf{q}_h^- & \text{if } \mathbf{x} < 0, \\ \mathbf{q}_h^+ & \text{if } \mathbf{x} > 0. \end{cases}$$

3

The solution to this problem, the intermediate solution $(\mathbf{q}_h^*(\mathbf{0}, t))$, is derived using the Rankine-Hugoniot jump condition as described in Refs. [16],[19],[10].The numerical fluxes $\mathbf{n} \cdot \mathbf{F}^* = \mathbf{n} \cdot \mathbf{F}(\mathbf{q}_h^*)$ are a function of the intermediate solution. After defining the numerical flux, the nodal basis and numerical flux are substituted into Equation 5 to obtain the semi-discrete form for each element as:

$$\mathbf{M}^k \frac{\partial \mathbf{u}_h^k}{\partial t} - \frac{1}{\rho} \left(\mathbf{S}_x^k \sigma_{xx_h}^k + \mathbf{S}_y^k \sigma_{xy_h}^k + \mathbf{S}_z^k \sigma_{xz_h}^k \right) = \mathbf{M}^k \left(g_{x_h}^k - \zeta_x \mathbf{u}_h^k \right) - \sum_{r=1}^{4} \mathbf{M}^{kr} \hat{\mathbf{F}}_u^{kr},$$

$$\mathbf{M}^k \frac{\partial \mathbf{v}_h^k}{\partial t} - \frac{1}{\rho} \left(\mathbf{S}_x^k \sigma_{xy_h}^k + \mathbf{S}_y^k \sigma_{yy_h}^k + \mathbf{S}_z^k \sigma_{yz_h}^k \right) = \mathbf{M}^k \left(g_{y_h}^k - \zeta_y \mathbf{v}_h^k \right) - \sum_{r=1}^{4} \mathbf{M}^{kr} \hat{\mathbf{F}}_v^{kr},$$

$$\mathbf{M}^k \frac{\partial \mathbf{w}_h^k}{\partial t} - \frac{1}{\rho} \left(\mathbf{S}_x^k \sigma_{xz_h}^k + \mathbf{S}_y^k \sigma_{yz_h}^k + \mathbf{S}_z^k \sigma_{zz_h}^k \right) = \mathbf{M}^k \left(g_{z_h}^k - \zeta_z \mathbf{w}_h^k \right) - \sum_{r=1}^{4} \mathbf{M}^{kr} \hat{\mathbf{F}}_w^{kr},$$

$$\mathbf{M}^k \frac{\partial \sigma_{xx_h}^k}{\partial t} - (\lambda + 2\mu) \mathbf{S}_x^k u_h^k - \lambda \mathbf{S}_y^k v_h^k - \lambda \mathbf{S}_z^k w_h^k = - \sum_{r=1}^{4} \mathbf{M}^{kr} \hat{\mathbf{F}}_{\sigma_{xx}}^{kr},$$

$$\mathbf{M}^k \frac{\partial \sigma_{yy_h}^k}{\partial t} - \lambda \mathbf{S}_x^k u_h^k - (\lambda + 2\mu) \mathbf{S}_y^k v_h^k - \lambda \mathbf{S}_z^k w_h^k = - \sum_{r=1}^{4} \mathbf{M}^{kr} \hat{\mathbf{F}}_{\sigma_{yy}}^{kr},$$ (6)

$$\mathbf{M}^k \frac{\partial \sigma_{zz_h}^k}{\partial t} - \lambda \mathbf{S}_x^k u_h^k - \lambda \mathbf{S}_y^k v_h^k - (\lambda + 2\mu) \mathbf{S}_z^k w_h^k = - \sum_{r=1}^{4} \mathbf{M}^{kr} \hat{\mathbf{F}}_{\sigma_{zz}}^{kr},$$

$$\mathbf{M}^k \frac{\partial \sigma_{xz_h}^k}{\partial t} - \mu \mathbf{S}_z^k u_h^k - \mu \mathbf{S}_x^k w_h^k = - \sum_{r=1}^{4} \mathbf{M}^{kr} \hat{\mathbf{F}}_{\sigma_{xz}}^{kr},$$

$$\mathbf{M}^k \frac{\partial \sigma_{yz_h}^k}{\partial t} - \mu \mathbf{S}_z^k v_h^k - \mu \mathbf{S}_y^k w_h^k = - \sum_{r=1}^{4} \mathbf{M}^{kr} \hat{\mathbf{F}}_{\sigma_{yz}}^{kr},$$

$$\mathbf{M}^k \frac{\partial \sigma_{xy_h}^k}{\partial t} - \mu \mathbf{S}_y^k u_h^k - \mu \mathbf{S}_x^k v_h^k = - \sum_{r=1}^{4} \mathbf{M}^{kr} \hat{\mathbf{F}}_{\sigma_{xy}}^{kr}.$$

The u_h^k, v_h^k, w_h^k, $\sigma_{xx_h}^k$, $\sigma_{yy_h}^k$, $\sigma_{zz_h}^k$, $\sigma_{xz_h}^k$, $\sigma_{yz_h}^k$, and $\sigma_{xy_h}^k$ are vectors representing all unknown variables at the nodal points x_i, with $i = 1$ to N_p. Note that all the mechanical properties in Equation 6 are defined in the interior element, except for the numerical flux terms. The second superscript r denotes the rth faces of ∂D^{kr} of the element D^k, where the number of faces of the tetrahedral element is four. The terms $\hat{\mathbf{F}}_u^{kr}$, $\hat{\mathbf{F}}_v^{kr}$, $\hat{\mathbf{F}}_w^{kr}$, $\hat{\mathbf{F}}_{\sigma_{xx}}^{kr}$, $\hat{\mathbf{F}}_{\sigma_{yy}}^{kr}$, $\hat{\mathbf{F}}_{\sigma_{zz}}^{kr}$, $\hat{\mathbf{F}}_{\sigma_{xz}}^{kr}$, $\hat{\mathbf{F}}_{\sigma_{yz}}^{kr}$, and $\hat{\mathbf{F}}_{\sigma_{xy}}^{kr}$ are the flux terms associated with the term $\mathbf{n} \cdot \left[\mathbf{F}^* - \mathbf{F}(\mathbf{q}_h^k) \right]$ over the element surface in the strong form (Equation 5). $\mathbf{M}^k$ is the element mass matrix, $\mathbf{S}_j^k$ are the element stiffness matrices in the j-directions, and $\mathbf{M}^{kr}$ are the element face matrices. More details on these matrices are given in Refs. [6, 18]. Having the semi-discrete form at hand, Equation 6 for the whole computational domain can be expressed in the form of ordinary differential equations as:

$$\frac{d\mathbf{q}_h}{dt} = \mathcal{L} \left(\mathbf{q}_h(t), t \right),$$ (7)

where $\mathbf{q}_h$ is the vector of all nodal solutions and $\mathcal{L}$ is the semi-discrete operator conducted over all elements. Finally, various methods can be used to integrate the time derivative in Equation 7. In this work, the fourth-order Runge-Kutta method with eight stages (RKF84) is used, which is described in Ref. [17]. The time-step (Δt) for the time integration is defined as:

$$\Delta t = \frac{C_{CFL} \cdot \min(r_{D^k})}{N^2 \cdot \max(c_p)}$$ (8)

where C_{CFL} is the Courant number, $\max(c_p)$ is the maximum longitudinal wave speed in the domain and $\min(r_{D^k})$ is the shortest element edge in the computational domain. The methodology on applying the force excitation and the boundary conditions can be found in Ref.[16].

4

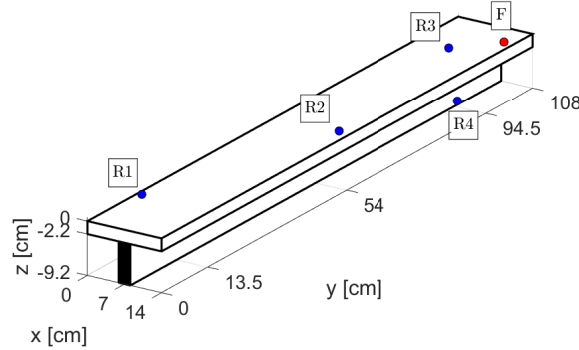# 3 Case studies

3.1. T-shaped structure

Figure 1: The case of the T-shaped structure that a fixed boundary condition is applied at the black coloured area. The red and blue dots denote the excitation and receiver locations, respectively.

As illustrated in Figure 1, the T-shaped structure is a simple structure consisting of two components with different mechanical properties, a vertical beam and a horizontal beam with dimensions [14 cm × 108 cm × 2.2 cm] and [2.2 cm × 108 cm × 7 cm], respectively. Its upper corner is at the origin of the coordinate system. The two components are glued to have a fixed connection at the interface on z = -2.2 [cm] surface, and the mechanical properties of the components are given in Table 1. Please note that the damping forces are the same in all directions $\zeta_x = \zeta_y = \zeta_z = \zeta$ and are assumed the same for both components.

Table 1: The mechanical properties of the constituting components of the T-shaped structure.

Component	Density [kg/m^3]	Young's Modulus [GPa]	Poisson's Ratio [-]	Damping force(ζ) [N · m^3/kg]
Vertical beam	616.1	2.39	0.3	10
Horizontal beam	720.8	3.57	0.3	10

A fixed BC is applied to the black coloured area shown in Figure 1, while remaining surfaces of the structure have free BCs. To excite the vibration, a point force (F) is applied at the coordinates (13, 101.25, 0) cm, marked with a red dot in Figure 1. To obtain the response of the structure, four receivers (R1-R4) are selected to record the velocities of the structure, as shown with blue dots in Figure 1. The receivers are selected in this manner since they are distributed at a different distance from the force location. The coordinates of the receivers are as follows R1=(1, 13.5, 0) cm, R2=(13, 54, 0) cm, R3=(7, 94.5, 0) cm, R4=(8.1, 94.5, -8.2) cm.

3.2. Scaled lightweight wooden floor

The scaled lightweight wooden floor (LWF) consists of a single panel as the top plate and seven joists to reinforce the plate, as shown in Figure 2. This case represents a more complex structure with many components and different mechanical properties as shown in Table 2. The top plate has dimensions [112 cm x 112 cm x 0.9 cm], and each joist has dimensions [108 cm x 2.2 cm x 7 cm]. The origin of the coordinate system is at the top corner of the plate, as shown in Figure 2. The joists are placed with an equal distance of 13.75 cm, with Joist 1 closest to the origin. The connections between the top floor and joists are fixed and all surfaces of the structure have the free BCs.

Table 2: Mechanical properties of the individual components of the scaled LWF structure.

Component	Density [kg/m^3]	Young's Modulus [GPa]	Poisson's Ratio [-]	Damping force(ζ) [N · m^3/kg]
Plate	670	3.70	0.3	20
Joist 1	583	1.89	0.3	20
Joist 2	565	2.06	0.3	20
Joist 3	559	2.07	0.3	20
Joist 4	571	2.14	0.3	20
Joist 5	577	2.16	0.3	20
Joist 6	589	2.39	0.3	20
Joist 7	577	2.10	0.3	20
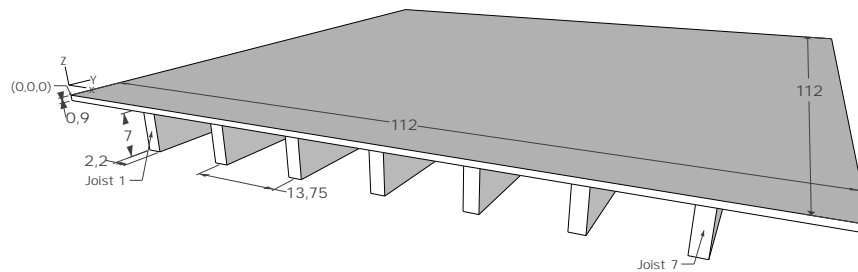
Figure 2: The scaled LWF structure, all dimensions are in centimetres.

The vibration behaviour of the scaled LWF structure under centre point excitation (F) is investigated. Four receivers C1-C4 were selected to observe the impact responses in this configuration. The coordinates of the force and receivers are as follows F=(56, 56, 0) cm, C1=(62.875, 42.25, 0) cm, C2 = (76.625, 28.5, 0), C3 = (83.5, 28.5, 0) cm, C4 = (97.25, 14.75, 0) cm.

4 Experimental Validation

4.1. Measurement set-up

The forced vibration experiments of the case studies presented in Section 3 are described here. The T-shaped structure is made of vertical and horizontal beams. These beams were glued to have a fixed connection. The vertical beam of the T-shaped structure was fixed by a steel clamp installed on a concrete slab as shown in Figure 3a. In the case of the scaled LWF structure, the structure was made of a top plate with seven joists. Each joist was attached to the bottom of the plate using nine screws that were spaced equally along the joists axial direction. By having closely adjacent screws, the joists were assumed to have a fixed connection to the top plate. In this study, the scaled-LWF structure was designed to have free BCs. To realise these BCs, several metal hooks were installed on the edge of the first and the last joist. Afterward, four rubber ropes connected these hooks to a crane machine to elevate the structure, as shown in Figure 3b. In both experimental cases, the acceleration signals were picked up by nine single-axis accelerometers (PCB 333B30). The force excitation was given by using an impact hammer (BK 8202) with a plastic tip. Also, National-Instruments acquisition systems (NI 9234 and cDAQ-9178) were used to capture the signals. All signals were captured for the duration of 7 s with a sampling frequency of 51.2 kHz.
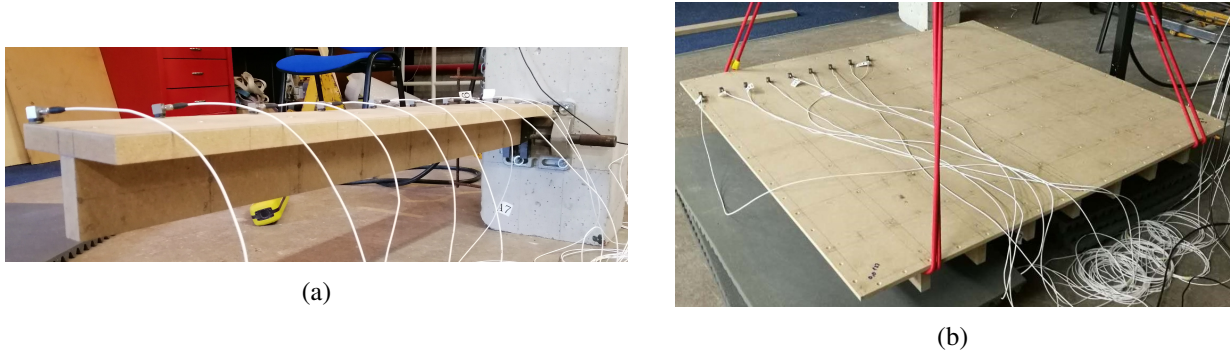
Figure 3: Measurement setup of (a) the T-shaped structure and (b) the scaled LWF structure.

4.2. Vibration data processing

In each case, the time-domain vibration signals were obtained from the measurements and the numerical computations. Subsequently, the signals were converted into frequency-domain data using the fast Fourier transform. In the frequency domain, the transfer function between velocity and force, i.e., mobility (Y_{ij}), was calculated to represent vibration responses of the individual case studies. The indices i, j refer to the velocity in the i-direction due to the force in the j-direction, and defined as:

$$Y_{ij}(f) = \frac{v_i(f)}{F_j(f)}. \tag{9}$$

In this study, two transfer mobilities are considered, $Y_{zz}(f)$ and $Y_{xz}(f)$. The velocity in the i-direction ($v_i(f)$) can be derived from the acceleration signals ($a_i(f)$) obtained by the accelerometer using the relation $v_i(f) = a_i(f)/j2\pi f$. To obtain the transfer mobilities from the experiment, the H1 estimator was used as shown in Ref.[15]. This estimator is used to reduce the influence of the noise on the measurements.

5   Results and Discussions

The results presented in this section use the following computational settings. The weighting coefficient ($C = 1$) is given, as shown in Equation 8. Lagrange polynomial functions of order ($N = 3$) is used, and an impact excitation on both structures is given by the external body force $g_z(t)$ in terms of the Ricker wavelet as: $g_z(t) = \left(0.5 - (\pi f_c(t - t_d))^2\right) e^{(\pi f_c(t-t_d))^2}$, with the centre frequency of $f_c = 250$ Hz and the centre time of $t_d = 7$ ms.
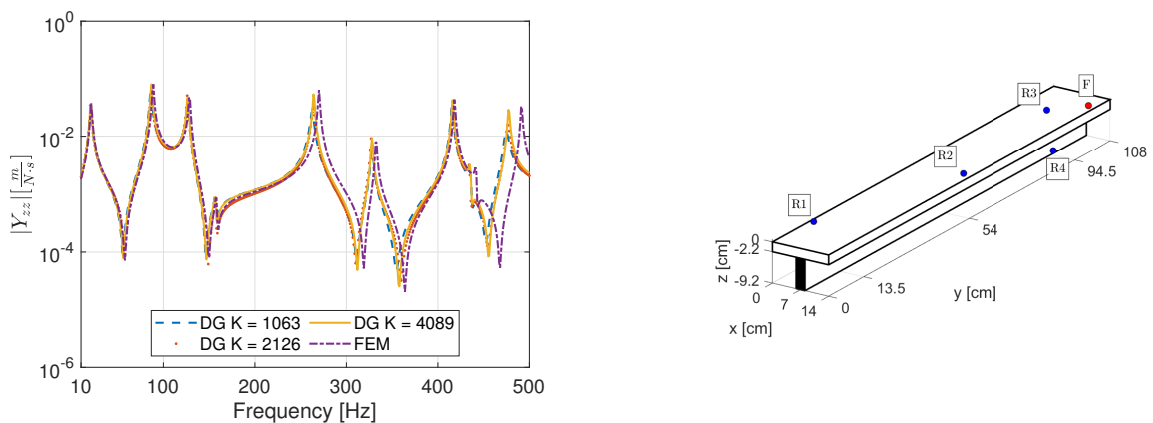
5.1. T-shaped structure

Figure 4: The mobilities at R2 position of the fixed BC configuration for different element numbers.

The nodal DG solution for the current configuration is shown in Figure 4. In this figure, three mobility curves Y_{zz} are shown at location R2. Each curve was obtained from the nodal DG model with a different number of elements, K = 1063, 2126, and 4089. The Table 3 lists all natural frequencies for each number of elements. It should be noted that the slowest wave in the T-shaped structure, the transverse wave, has a velocity of 1221.5 m/s. This means that the minimum wavelength at 500 Hz is about 2.4 m, and the structure seems oversampled by the discretisation. However, since the structure has a small thickness which is 2.2 cm, the discretisation should maintain a limited skewness of the tetrahedral element to have a good numerical result. Moreover, the changes of the natural frequencies between all different element number are less than 2 Hz and is assumed the results have converged. The DG results of K = 4089 is compared with the measurement results. In addition, the same case is simulated with FEM using COMSOL Multiphysics 5.6 [1] in frequency domain by solving the linear elasticity equations. The comparison with the FEM solution shows that the nodal DG approach has a maximum difference of 15 Hz at the highest natural frequency. This is caused by the discontinuity of BCs at y = 0 cm and z = -2.2 cm. In the FEM, the solution is continuous at the edges of the elements, but the nodal DG solution can have two solutions at the same position due to its discontinuous elements.
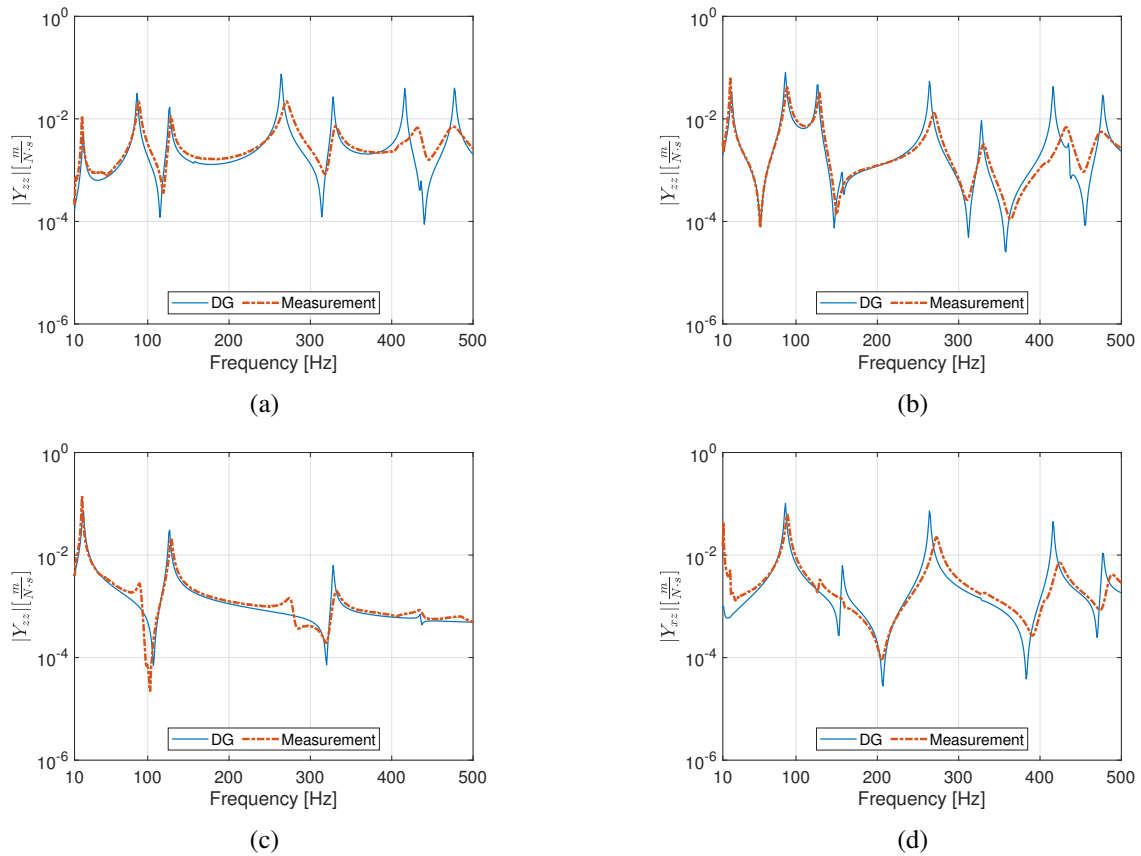

Figure 5: Mobilities of the T-shaped structure obtained by the nodal DG method and the measurements at the positions (a) R1, (b) R2, (c) R3, and (d) R4.

The mobilities at receivers R1-R4 are shown in Figures 5. It can be seen that the mobilities obtained from the nodal DG method closely match those obtained from the measurement. Table 3 lists all the discrepancies of the natural frequencies, with the sixth natural frequency having a maximum absolute frequency difference $|\Delta f_n| = 16.3$ Hz from the measured value, which is 3.8% deviation. The other natural frequencies have smaller absolute differences. It is assumed that these differences are due to the isotropic assumption of the vertical and horizontal beams in the nodal DG model, since it is known that the MDF material has a slight orthotropic property. The magnitude discrepancies are caused by inadequacy of internal damping properties. The given

constant viscous damping cannot capture the frequency-dependent damping properties of the structure. From Figure 5, it can be seen that the magnitude of mobilities obtained by the nodal DG method and the measurements is of the same order for the frequencies below 150 Hz. However, the attenuation increases more rapidly with frequency, in the experimental results than in the computational results. In Figure 5d, the mobility in the x-direction at position R4 is shown. This mobility has the same magnitude as the mobility in the z-direction at the other positions (R1-R3) due to the body force in the z-direction.

Table 3: Natural frequencies at the T-shaped structure obtained from the nodal DG method and measurements at position R2.

Index	Natural frequency [Hz]				$|\Delta f_n|$	
	K = 1063	K = 2126	K = 4089	Measurement	[Hz]	[%]
1	21.0	20.0	20.0	19.3	0.7	3.6
2	86.0	87.0	87.0	89.0	2.0	2.2
3	127.0	126.0	126.0	128.6	2.6	2.0
4	263.0	264.0	264.0	269.9	5.9	2.2
5	328.0	327.0	328.0	330.6	2.6	<1.0
6	415.0	416.0	416.0	432.3	16.3	3.8
7	475.0	476.0	477.0	475.7	2.7	<1.0

5.2. Scaled lightweight wooden floor

Three mobility curves Y_{zz} at position C1 excited by the force at the centre position are displayed in Figure 6. It should be noted that the thickness of the plate structure is 0.9 cm,and to maintain a good skewness of the element, a sufficient number of elements is needed (average skewness for K = 6918 is 0.33). The average skewness of the element is expected to be more than 0.3 to have a good tetrahedral element. In this case, the solution from K = 13685 is taken as the comparison to the measurement results. All natural frequencies below 300 Hz are tabulated in Table 4.
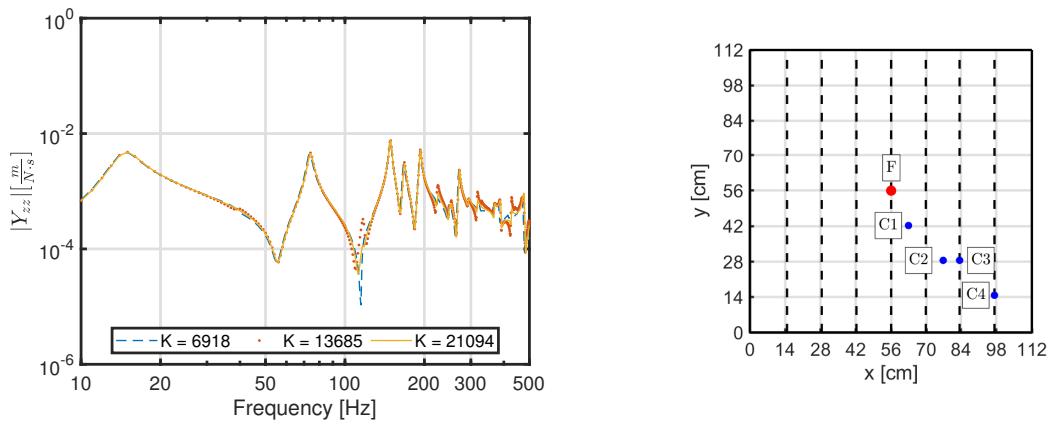

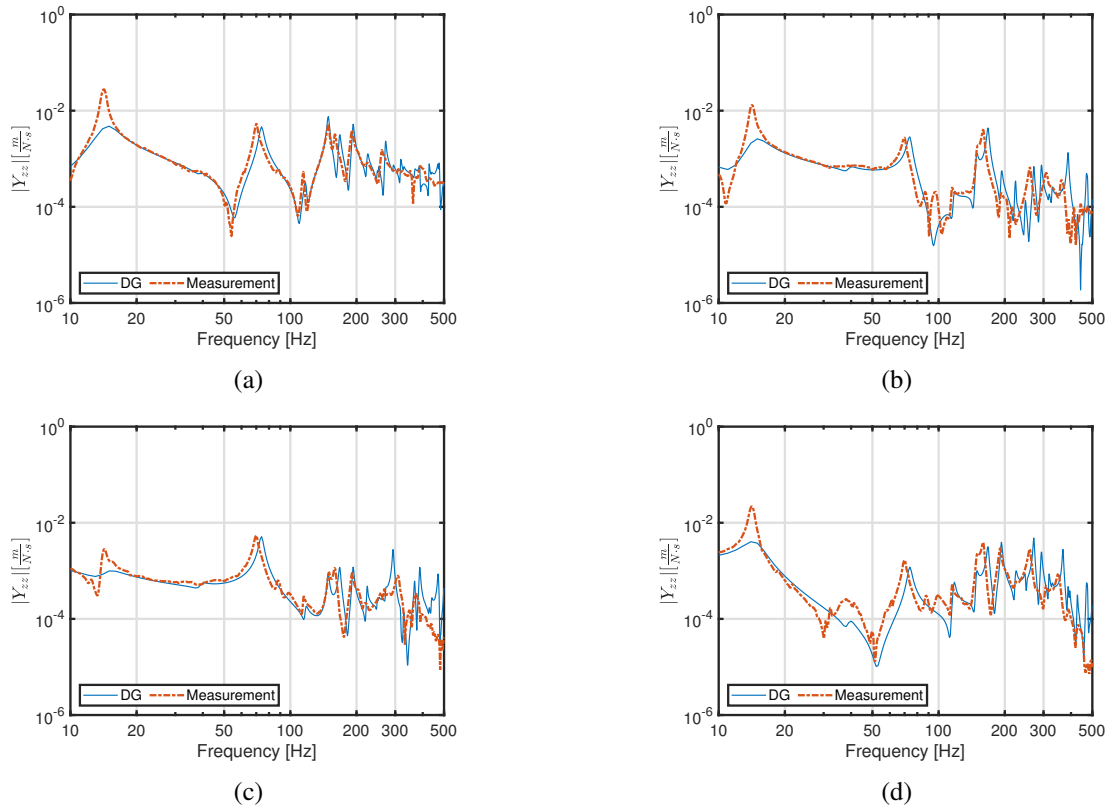Figure 6: Numerical solutions of the scaled LWF at position C1 for different element numbers.

9

Figure 7: Mobilities of the scaled LWF structure obtained by the nodal DG method and the measurements at the positions (a) C1, (b) C2, (c) C3, and (b) C4.

Figure 7 shows the mobilities at positions C1-C4. As mentioned in Section 2, these points are gradually further away from the excitation point. All mobilities obtained by the nodal DG method agree well with the measurement results, especially in the frequency range 20-250 Hz. Outside this range, the discrepancy of the measurement results and the simulation results increases. Similar to the previous case, the constant damping is a reason for this, where the model does not capture the frequency-dependent damping of the structure. It can be seen that the first natural frequency at 15 Hz is heavily damped in DG and the applied constant damping is too high for this mode. In contrast, above 250 Hz the damping from the experimental results becomes higher and the location of the natural frequencies is no longer discernible. Another source of discrepancy is the connection between plate and joists. These components are connected by nails without glue, and modelling these connections as fixed connections along the contact interface can lead to inaccuracies.

Table 4: Natural frequencies at the scaled LWF structure obtained from the nodal DG method and measurements at position C1.

Index	Natural Frequency [Hz]				$|\Delta f_n|$	
	K = 6918	K = 13685	K = 21094	Measurement	[Hz]	[%]
1	15.0	15.0	15.0	14.1	0.9	6.4
2	73.0	74.0	74.0	70.1	3.9	5.6
3	149.0	149.0	149.0	148.9	0.1	<1.0
4	167.0	168.0	168.0	159.6	8.4	5.3
5	193.0	193.0	193.0	190.9	2.1	1.1
6	270.0	271.0	272.0	260.9	10.1	3.9

6   Conclusions

In this study, the nodal DG method is applied to model the vibration of a T-shaped structure and a scaled lightweight wooden floor. These structures are made of several components that have different material properties resulting in constant piece-wise material properties in the computational domain. The numerical fluxes in the materials with the piece-wise constant properties in the computational domain are derived by the Rankine-Hugoniot jump condition. To validate the numerical results, the mobility of the structures is calculated and compared with results from an experimental study. The agreement is good regarding the natural frequencies, with a maximum difference of less than 4 % for the T-shaped structure in the range below 500 Hz, and 6.4 % for the scaled LWF structure in the range below 300 Hz. In comparison, the adopted damping approach is insufficient to represent a broad frequency range. In future work, incorporating the frequency-dependent damping into nodal DG model is important. Moreover, the extension into anisotropic properties of the model could be essential especially for wooden based structures.

Acknowledgements

References

[1] AB, C. Comsol multiphysics ® version 5.4., 2018.

[2] BRUNSKOG, J., AND CHUNG, H. Non-diffuseness of vibration fields in ribbed plates. *The Journal of the Acoustical Society of America 129*, 3 (2011), 1336–1343.

[3] BRUNSKOG, J., AND HAMMER, P. Prediction models of impact sound insulation on timber floor structures a literature survey. *Building Acoustics 7*, 2 (2000), 89–112.

[4] DECKERS, E., ATAK, O., COOX, L., DAMICO, R., DEVRIENDT, H., JONCKHEERE, S., KOO, K., PLUYMERS, B., VANDEPITTE, D., AND DESMET, W. The wave based method: An overview of 15 years of research. *Wave Motion 51*, 4 (2014).

[5] FOX, C., AND CHUNG, H. Modeling low-frequency vibration in light-weight timber floor/ceiling systems. *The Journal of the Acoustical Society of America 145*, 2 (2019), 831–846.

[6] HESTHAVEN, J. *Nodal discontinuous Galerkin methods : algorithms, analysis, and applications*. Springer, New York, 2008.

[7] HOPKINS, C. Vibration transmission between coupled plates using finite element methods and statistical energy analysis. part 1: Comparison of measured and predicted data for masonry walls with and without apertures. *Applied Acoustics 64*, 10 (2003), 955–973.

[8] HOPKINS, C., CRISPIN, C., POBLET-PUIG, J., AND GUIGOU-CARTER, C. Regression curves for vibration transmission across junctions of heavyweight walls and floors based on finite element methods and wave theory. *Applied Acoustics 113* (2016), 7–21.

[9] JOHANSSON, C. Low-frequency impact sound insulation of a light weight wooden joist floor. *Applied Acoustics 44*, 2 (1995), 133–147.

[10] LEVEQUE, R. J. *Finite volume methods for hyperbolic problems*. Cambridge Unversity Press, Cambridge, 2004.

[11] MODAVE, A., ST-CYR, A., AND WARBURTON, T. GPU performance analysis of a nodal discontinuous galerkin method for acoustic and elastic models. *Computers & Geosciences 91* (2016), 64–76.

[12] POBLET-PUIG, J., AND GUIGOU-CARTER, C. Using spectral finite elements for parametric analysis of the vibration reduction index of heavy junctions oriented to flanking transmissions and en-12354 prediction method. *Applied Acoustics 99* (2015), 8–23.

[13] SAKUMA, T., SAKAMOTO, S., AND OTSURU, T. *Computational Simulation in Architectural and Environmental Acoustics*. Springer Japan, 2014.

[14] SHI, X., AND SHI, D. Free and forced vibration analysis of t-shaped plates with general elastic boundary supports. *Journal of Low Frequency Noise, Vibration and Active Control 37*, 2 (2018), 355–372.

[15] SHIN, K., AND HAMMOND, J. *Fundamentals of signal processing for sound and vibration engineers*. Wiley, 2008.

[16] SIHAR, I., AND HORNIKX, M. Implementation of the nodal discontinuous galerkin method for the plate vibration problem using linear elasticity equations. *Acta Acustica united with Acustica 105*, 4 (2019), 668–681.

[17] TOULORGE, T. *Efficient Runge-Kutta discontinuous Galerkin methods applied to aeroacoustics*. PhD thesis, Katholieke Universiteit Leuven, 2012.

[18] WANG, H., SIHAR, I., PAGÁN MUÑOZ, R., AND HORNIKX, M. Room acoustics modelling in the time-domain with the nodal discontinuous Galerkin method. *The Journal of the Acoustical Society of America 145*, 4 (2019), 2650–2663.

[19] WILCOX, L. C., STADLER, G., BURSTEDDE, C., AND GHATTAS, O. A high-order discontinuous Galerkin method for wave propagation through coupled elastic-acoustic media. *Journal of Computational Physics 229*, 24 (2010), 9373–9396.